676a (alumina) is well suited to assessing instrument response because it is non-orienting and of high purity. Alumina is of lower symmetry than either silicon or lanthanum hexaboride; it has a considerable number of diffraction lines and has well established structure parameters. A Rietveld analysis of SRM 660c, however, yields the IPF in terms of code-specific profile shape terms and verifies that peak-position-specific aspects of the equipment and analysis are working correctly.

The instrument response may be evaluated with the more conventional data-analysis methods with use of SRM 1976b. Measurements of peak intensities are obtained from the test instrument, typically by profile fitting, and compared with the certified values. However, the use of SRM 1976b with diffraction equipment with different optical configurations may require the application of a bias to the certified values to render them appropriate for the machine to be qualified. This bias is needed to account for differences in the polarization effects from the presence, absence and character of crystal monochromators. The polarization factor for a diffractometer that is not equipped with a monochromator is (Guinier, 1994)

$$\frac{1+\cos^2 2\theta}{2}. \tag{3.1.4}$$

The polarization factor for a diffractometer equipped with only an incident-beam monochromator is (Azároff, 1955)

$$\frac{1+\cos^2 2\theta_m \cos^2 2\theta}{1+\cos^2 2\theta_m}, \tag{3.1.5}$$

where $2\theta_m$ is the 2θ angle of diffraction for the monochromator crystal. The polarization factor for a diffractometer equipped with only a diffracted-beam post-monochromator is (Yao & Jinno, 1982)

$$\frac{1+\cos^2 2\theta_m \cos^2 2\theta}{2}, \tag{3.1.6}$$

where $2\theta_m$ is the 2θ angle of the monochromator crystal. Equations (3.1.5) and (3.1.6) are appropriate when the crystal has an ideal mosaic structure, *i.e.* the diffracting domains are uniformly small and, therefore, the crystal is diffracting in the kinematic limit. This is in contrast to a 'perfect' crystal, which would diffract in accordance with dynamical scattering theory. Note that equations (3.1.5) and (3.1.6) both have the $\cos^2 2\theta_m$ multiplier operating on the $\cos^2 2\theta$ term. Since this multiplier is less than unity, the intensity change on machines equipped with a monochromator exhibits a weaker angular dependence.

The certification data for SRM 1976b were collected with the NIST machine equipped with the Johansson IBM and a scintillation detector. The simplified IPF of this machine is advantageous for the accurate fitting of the profiles and, therefore, intensity measurement. The validity of the 'ideal mosaic' assumption embodied in equation (3.1.5) was evaluated using this diffractometer; the validity of equation (3.1.6) was evaluated with data from the machine configured with the post-monochromator. With respect to equation (3.1.5), for a Ge crystal (111) reflection, $2\theta_m$ was set to 27.3°; with regard to equation (3.1.6), for a pyrolytic graphite crystal (0002) basal-plane reflection, $2\theta_m$ was set to 26.6°. Rietveld analyses of data from SRMs 660b, 1976b and 676a included a refinement of the polarization factor, modelled according to equations (3.1.5) and (3.1.6) in *TOPAS*, and yielded fits of high quality, indicating that these models were appropriate for these crystals and configurations. Equations (3.1.4), (3.1.5) and (3.1.6) were used to bias the certified values to correspond to those of alternative configurations. These values are included in the SRM 1976b CoA as ancillary data.

3.1.6. Instrument calibration

The calibration procedure has traditionally involved the comparison of measurements from a reference (an SRM) with those of the test instrument. However, the exact form of this comparison depends upon the data-analysis procedure to be used. A classical calibration, permitting qualitative analyses and lattice-parameter refinement, can be readily performed as per Fig. 3.1.26. These data are fitted with a polynomial that describes the 2θ error correction that is then applied to subsequent unknown samples. Furthermore, with this calibration method, the actual form of the curve of Fig. 3.1.26 is largely irrelevant. As the data-analysis methods become more advanced, physical models are chosen to replace analytical PSFs. The calibration is then based upon the observation that the machine performance does indeed correspond to the models used, and that acceptable values for refined parameters describing the experiment are obtained from an analysis of data from an SRM. A systematic approach to instrument calibration with a full evaluation of the data, including those obtained from the empirical methods shown in Figs. 3.1.26 and 3.1.27, results in the ability to use the advanced methods in a rational manner and obtain results in which one can have confidence. The advanced methods, while more complex to use and requiring a much more extensive instrument calibration process, reward the user with a sample characterization of greater breadth and reduced measurement uncertainty.

Consider the $\Delta(2\theta)$ curve illustrated in Fig. 3.1.26. The *y*-axis values are the differences between the peak positions computed from the certified lattice parameter of SRM 660b and those of each observed profile determined *via* a second-derivative-based peak-location algorithm. Therefore, each of the $\Delta(2\theta)$ data points plotted on Fig. 3.1.26 were determined independently. It is immediately apparent that the data follow a smooth, monotonic curve with no substantive outliers. Discontinuities or non-monotonicity would typically indicate mechanical difficulties with the equipment, such as loose components or problems with the goniometer assembly. Evaluation of independently determined data such as these is critical to verifying that there are no 'high-frequency' difficulties with the equipment that would otherwise be hidden or smoothed out with the use of methods that apply models or constraints across the entire 2θ range, such as a Rietveld analysis. The $\Delta(2\theta)$ values were fitted with a third-order polynomial that is also illustrated in Fig. 3.1.26. Consideration of the deviation values between the observations and the third-order fit indicates a random or 'top hat' distribution with a maximum excursion of $\pm 0.0025°$ 2θ; this provides further evidence that a machine is operating properly.

FPAPC was used to generate simulated data, which were then analysed using the same second-derivative algorithm as was applied to the raw data. The aforementioned optical setup of the NIST instrument was used in the as-configured simulation (see the caption for Fig. 3.1.26), while the high-resolution and low-resolution data were simulated with a 50% increase or decrease of the incident and Soller slit angles. For the 'high-resolution' and 'low-resolution' data, third-order polynomial fits to the $\Delta(2\theta)$ values are displayed in Fig. 3.1.26; for the 'as-configured' data, the Δ values themselves are indicated. The correspondence between the simulation and observation indicates that trends in the data can be readily explained in the context of the aberration functions discussed in Section 3.1.1 and that such a machine can

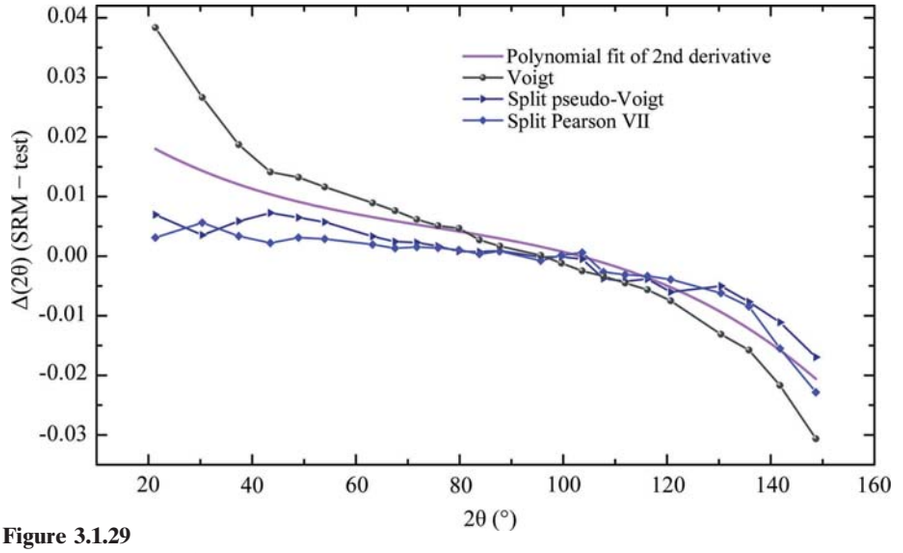

Figure 3.1.29
Comparison of $\Delta(2\theta)$ curves determined with profile fitting of SRM 660b data without the use of any constraints, as a function of 2θ.

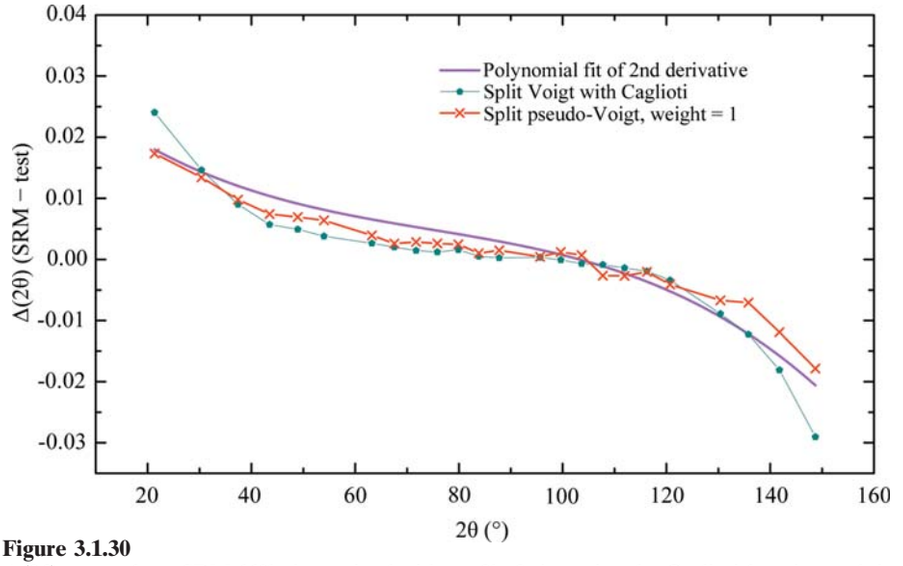

Figure 3.1.30
$\Delta(2\theta)$ curves from SRM 660b determined with profile fitting using the Caglioti function and the unconstrained split pseudo-Voigt PSF with uniform weighting.

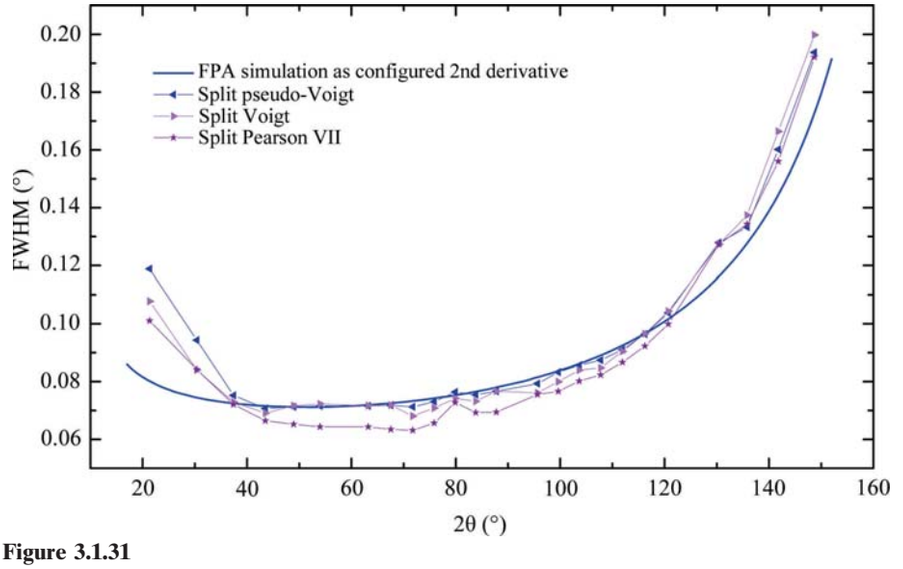

Figure 3.1.31
FWHM data from SRM 660b using various split PSFs fitted without constraints.

generate data for successful analysis with the FPA method, *i.e.* the metrological loop is closed. At low 2θ the profiles are displaced to low angle by the effects of the flat specimen error and axial divergence. The $\Delta(2\theta)$ curve crosses the zero point at approximately 100° 2θ where the profiles are largely symmetric; the slight asymmetry to low angle caused by the flat specimen error is somewhat offset by asymmetry of the emission spectrum at high angles. At higher 2θ the profiles are displaced to high angle by the combined effects of axial divergence and the asymmetry of the emission spectrum. As illustrated with the simulations at lower and higher resolution, the experimental curve of Fig. 3.1.26 would either flatten out or become steeper, respectively, with changes in instrument resolution. Given the uniformity of the data and overall plausibility of this $\Delta(2\theta)$ curve, the third-order polynomial fit is used as a reference against which the merits of other techniques can be judged.

It should also be noted that the data and method shown Fig. 3.1.26 constitute the 'low-hanging fruit' of powder diffraction. Data analogous to those of Fig. 3.1.26 can be used to correct peak positions of unknowns *via* either the internal- or external-standard method using a polynomial fit. The external-standard method, however, cannot account for specimen displacement or sample-transparency effects; these require use of the internal-standard method, which is the same procedure but applied to a standard admixed with the unknown. Either of these methods will correct for instrumental aberrations regardless of their form; the nature of the curve of Fig. 3.1.26 need only be continuous to permit modelling with a low-order polynomial. Studies performed in conjunction with the International Centre for Diffraction Data (ICDD) demonstrate that the use of the internal-standard method routinely yields results that are accurate to parts in 10^4 (Edmonds *et al.*, 1986). Fawcett *et al.* (2004) demonstrated the direct relationship between the use of standards, with the vast majority of analyses being performed *via* the internal- or external-standard methods, and the number of high-quality starred patterns in the ICDD database. Thus, the community's collective ability to perform the most routine of XRPD analyses, qualitative analysis, has been greatly enhanced over the past 30 or so years by these most basic methods and the use of SRMs.

The $\Delta(2\theta)$ and FWHM calibration curves shown in Figs. 3.1.27–3.1.31 were determined *via* profile fitting, using several PSFs,

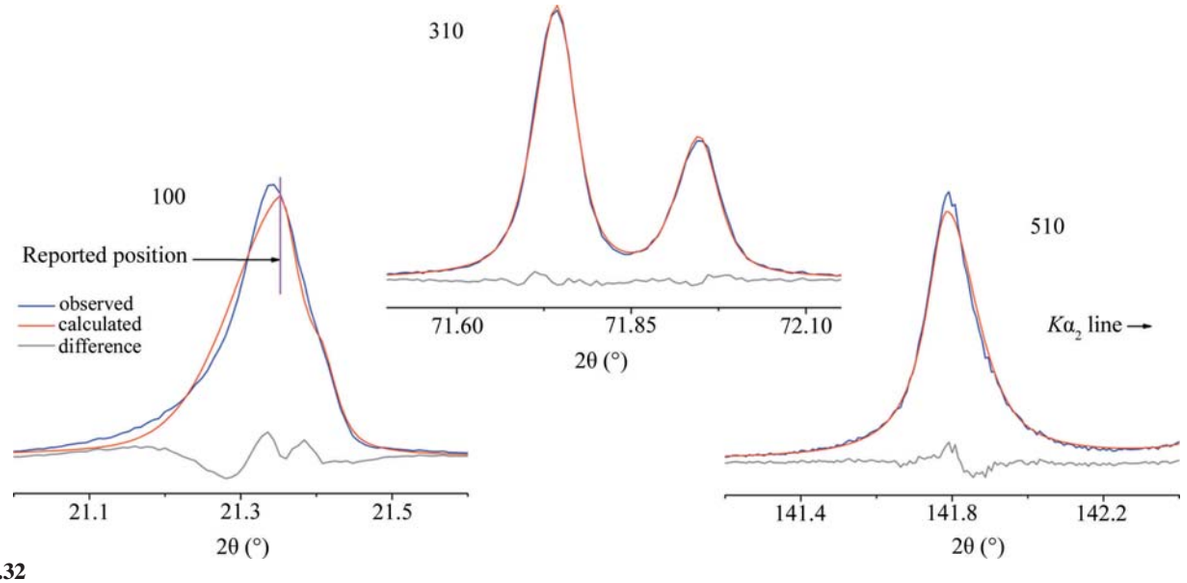

Figure 3.1.32
Fits of the split pseudo-Voigt PSF to the low-angle 100, mid-angle 310 and high-angle 510 lines from SRM 660b illustrating the erroneous peak position and FWHM value reported for the 100 and 510 lines, respectively.

of the same raw data from SRM 660b used to generate Fig. 3.1.26. In general, results from the three commercial codes were in close correspondence. When used on a split PSF, the Caglioti function was applied independently to the left and right FWHM values. A five- to seven-term Chebyshev polynomial was used for modelling the background in these refinements. The goodness of fit (GoF) (which is the square root of reduced χ^2) residual error term of the refinements ranged from 1.6 to 1.9, with the unconstrained refinements yielding the slightly improved fits to the data. Fig. 3.1.32 illustrates the fit quality of typical results using the split pseudo-Voigt PSF. However, as will be demonstrated, the more plausible parameters, particularly in the context of the FWHM values, were often obtained with the more constrained refinements.

The results from the fitting of the Voigt PSF provide a reference for consideration of the $\Delta(2\theta)$ data of Fig. 3.1.29. The use of any of the symmetric PSFs considered here, with or without the Caglioti constraint, resulted in curves virtually identical to the one displayed in Fig. 3.1.29 for the Voigt PSF. Not surprisingly, the symmetric PSF performs quite well in the mid-angle region where the profiles are symmetric but will report an erroneous position in the direction of the asymmetry, when it is present. However, the opposite effect was observed with the use of any of the split PSFs, as can be seen in Figs. 3.1.29 and 3.1.32. When two HWHM values are refined, the larger HWHM value will shift the reported peak position in the direction of the smaller one. This effect can be readily observed in the fit quality of the low-angle 100 reflection displayed in Fig. 3.1.32. The spilt PSFs yield results that reflect an overly asymmetric profile; thus the reported peak positions are displaced to high angle at 2θ angles below 100°, and to low angle at 2θ angles above 100°. Curiously this effect was markedly reduced in one of the commercial computer codes (not shown) and was the sole difference observed between them when the models were equivalent. It is apparent that subtleties in implementation of an ostensibly identical PSF and minimization algorithm (the Marquardt algorithm) can result in dramatic differences in results. Careful examination of the fit quality is required to assess the reliability of profile-fitting results. The data of Fig. 3.1.29 indicate that errors in peak position of up to 0.015° 2θ are plausible with profile fitting of these data with these PSFs. In contrast to its use with symmetric PSFs, the Caglioti function will improve results when using split PSFs (Fig. 3.1.30).

Consideration of the issues related to profile fitting shown in Fig. 3.1.32 led to the conjecture that fitting the data with a uniform weighting as opposed to Poisson statistical weighting might result in more accurate determination of the peak position and FWHM parameters. (In the vast majority of circumstances this approach would never be used, because the integrated intensity is a critical metric.) This was tried, and resulted in considerable success. Fig. 3.1.30 displays data from the use of split pseudo-Voigt that are in very good agreement with second-derivative values.

Experimental and simulated values of the FWHM are displayed in Figs. 3.1.27 and 3.1.31. Data from the profile refinements performed without the use of the Caglioti function, displayed in Figs. 3.1.27 and 3.1.31, yield independently determined measures of the FWHM. Again, the lack of scatter and the continuity of these FWHM values are consistent with proper operation of the instrument, *i.e.* an absence of 'high-frequency' problems. The basic trends are also consistent with the instrument optics: at low 2θ the observed increase in FWHM is due to both the flat specimen and axial divergence aberrations, while at high 2θ angular dispersion dominates and a substantial increase in FWHM with $\tan\theta$ is apparent. The FPA simulations were performed using the settings for high and low resolution. The FWHM values were determined numerically from the simulated patterns; no PSF was used. As shown with the simulated data, the degree of upturn at low 2θ increases with a decrease in instrument resolution and *vice versa*. Angular-dispersion effects, however, are less dependent on the instrument configuration; FWHM values tend towards convergence at high 2θ (Fig. 3.1.27).

As seen in Fig. 3.1.27, above 40° 2θ the Voigt and split-Voigt PSFs give similar values for the FWHM and a fairly accurate representation of instrument performance. It was observed that with regard to the correlation between FWHM values for split *versus* symmetric PSFs, the other PSFs behaved in an analogous manner to the Voigt (not shown): above 40° 2θ the values reported for the FWHM from split *versus* symmetric PSFs are nearly identical. From Fig. 3.1.31, the split Pearson VII PSF underestimates the FWHM throughout the mid-angle region; this error was duplicated with the use of the symmetric Pearson VII

PSF (not shown). When fitted with uniform weighting, however, these FWHM data from the Pearson VII PSF fell quite precisely (not shown) on the simulated curve. Below 40° 2θ, a split PSF will provide results that overestimate true FWHM values, as shown in Figs. 3.1.27 and 3.1.31. The cause for this is analogous to that discussed for the $\Delta(2\theta)$ values, and can be readily observed in the fit quality displayed in Fig. 3.1.32 for the low-angle 100 reflection. In accounting for the asymmetry to low angle, the FWHM of the observed profile is substantially overestimated by the calculated one. With all PSFs, the high-angle FWHM values are observed to be overestimated, as shown in Figs. 3.1.27 and 3.1.31; the problem is exacerbated with the use of the Caglioti function. Inspection of the fit quality of the high-angle 510 line shown in Fig. 3.1.32 indicates that there are two contributions to this effect: one is that the PSF cannot model the shape of the high side of the profile; the other is that the height of the profile is underestimated. These two effects, particularly the inability of the PSF to correctly model the height of the profile, were observed with all of the other PSFs considered here.

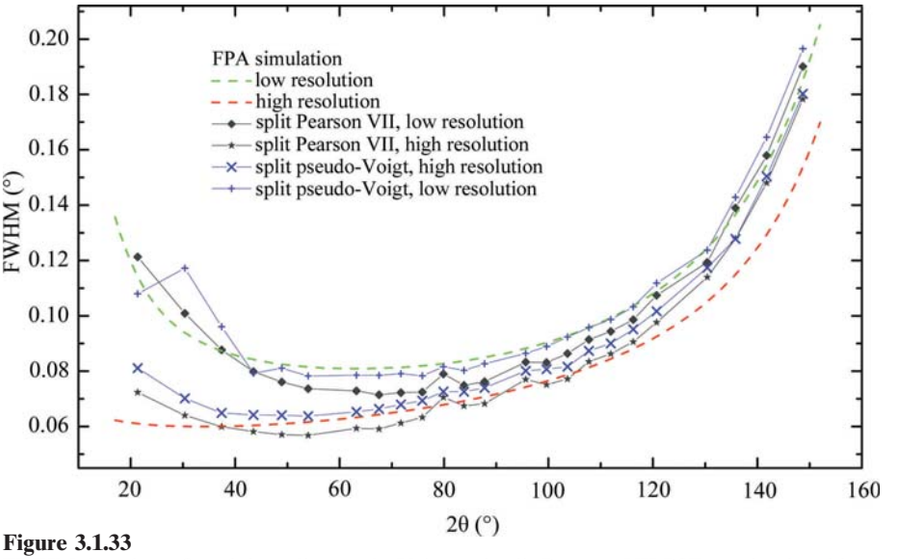

Figure 3.1.33
FWHM data from fits of the split pseudo-Voigt and split Pearson VII PSFs to simulated low- and high-resolution data.

The use of the pseudo-Voigt PSF with the Caglioti function results in a reasonable fit to the FWHM values of the observation; however, the breadth of the high-angle lines is overestimated. The *U*, *V* and *W* terms of the Caglioti function vary in a specific manner to account for various physical effects (*e.g.* see Fig. 3.1.27): the *U* term, in tan θ, accounts for angular dispersion; the *W* term describes the 'floor' and the *V* term accounts for the reduction of the FWHM values in the mid-2θ region. Therefore, the *U* and *W* terms should refine to positive values, while the *V* term should tend to a negative value; negative values for *V* were, indeed, obtained in these analyses. *V* should be constrained to negative values or set to zero, as positive values for *V* are non-physical. With an instrument configured for high resolution, however, values of $V = 0$ are entirely reasonable as the trend towards an upturn in FWHM at low 2θ angle will be suppressed.

To some extent, the difficulties in determining profile positions through the use of these PSFs can be ascribed to the Cu $K\alpha_1/K\alpha_2$ doublet as it is stretched by angular dispersion. The pattern can be thought of as divided into three regions, each of which will confound fitting procedures in a different manner: the low-2θ range, where profiles can be considered as a peak with a shoulder, the mid-2θ range (perhaps 40 to 110° 2θ), where the profiles can be considered as a doublet, and the high-angle region where they are two distinct peaks. This 'three-region' consideration is compounded by the direction and severity of the asymmetry in these profiles. The data shown in Fig. 3.1.27 largely correspond to the problematic effects of angular dispersion in the context of these three 2θ regions. These effects are particularly apparent, as shown in Fig. 3.1.31, with the use of the Pearson VII function: over-estimation of FWHM values occurs at low 2θ, underestimation occurs in the mid-2θ region, and credible values are obtained at high angle. The use of the Caglioti function is effective in addressing the more extreme excursions from plausible FWHM values. Fig. 3.1.28 shows the left and right HWHM values for SRM 660b using the split pseudo-Voigt PSF refined with uniform weighting. For reasons discussed in Section 3.1.2, the degree, direction and point of crossover in the profile asymmetry indicated in Fig. 3.1.28 are in correspondence with expectation and the previously discussed results from these data from SRM 660b.

To consider the impact of instrument resolution on the use of analytical PSFs for the determination of FWHM values, the simulated high-resolution and low-resolution data were analysed *via* profile fitting. Fig. 3.1.33 shows the results from the use of the split Pearson VII and spilt pseudo-Voigt PSFs. The data of Fig. 3.1.33 indicate an effect that is dependent on the PSF used. The performance of the split Pearson VII PSF is observed to improve with instrument resolution; FWHM values from the narrower profiles are observed to correspond with expectation in the low- and mid-angle regions, while substantial deviation is noted with the broader profiles. This is counter to expectation, as broader profiles are generally easier to fit than narrow ones. The performance of the split pseudo-Voigt PSF is observed to degrade marginally with either an increase or decrease in instrument resolution. Curiously, the breadths of the profiles in the high-resolution data are overestimated, while those in low-resolution data are largely underestimated. Both PSFs do quite poorly in fitting the high-angle data from the high-resolution setting. These observations emphasize the need to scrutinize the results with an examination of the fit quality, as per Fig. 3.1.32.

When the IPF is simplified with the use of a Johansson IBM, analytical PSFs can provide an excellent fit to the observations. Fig. 3.1.34 shows the fit quality of the split Pearson VII PSF to (high-quality) peak-scan data. The split Pearson VII PSF consistently provides a better fit to IBM data than either the split Voigt or split pseudo-Voigt PSFs. Note that the asymmetry exhibited by the profiles follows the same trends as were outlined previously, but to a much reduced extent because of the extended incident-beam path length and the resulting reduction in the effects of axial divergence. Fig. 3.1.35 shows the $\Delta(2\theta)$ calibration curves that were obtained as per the procedures outlined for Fig. 3.1.29. Indeed, the trends that are followed, and the reasons why, are largely analogous to those of Fig. 3.1.29, but to a much reduced extent because of the reduced profile asymmetry. Use of symmetric PSFs yields reported peak positions that are shifted in the direction of the asymmetry, while use of split PSFs yields positions shifted in the opposite direction owing to the fitted profiles displaying excessive levels of asymmetry. One notes the complete failure of the split pseudo-Voigt, split Voigt (not shown)

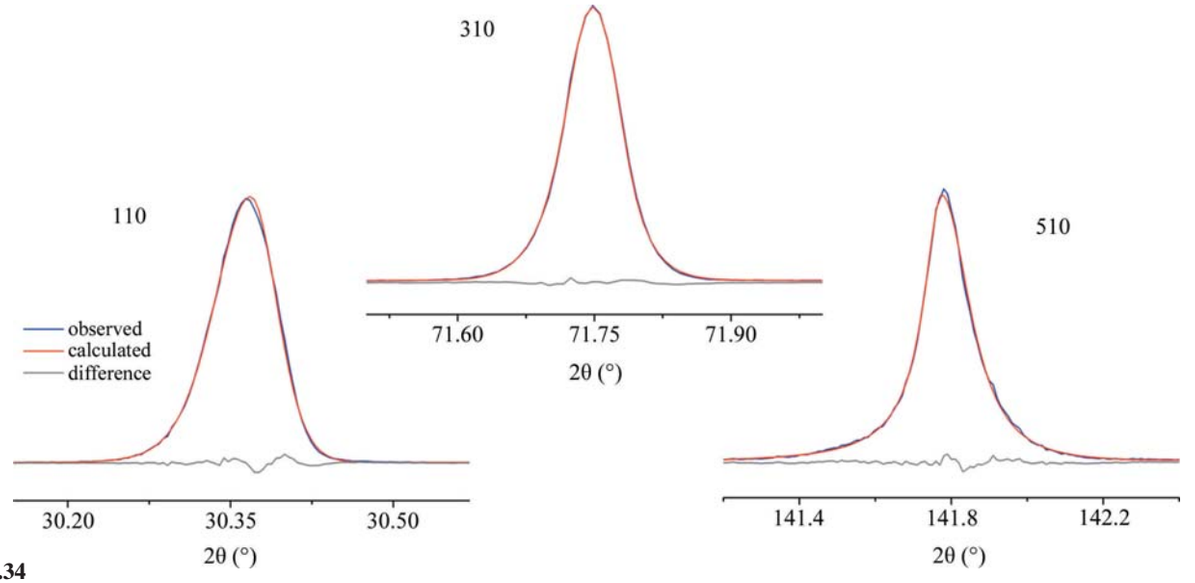

Figure 3.1.34
Fits of a split Pearson VII PSF to data from SRM 660b collected using a Johansson IBM.

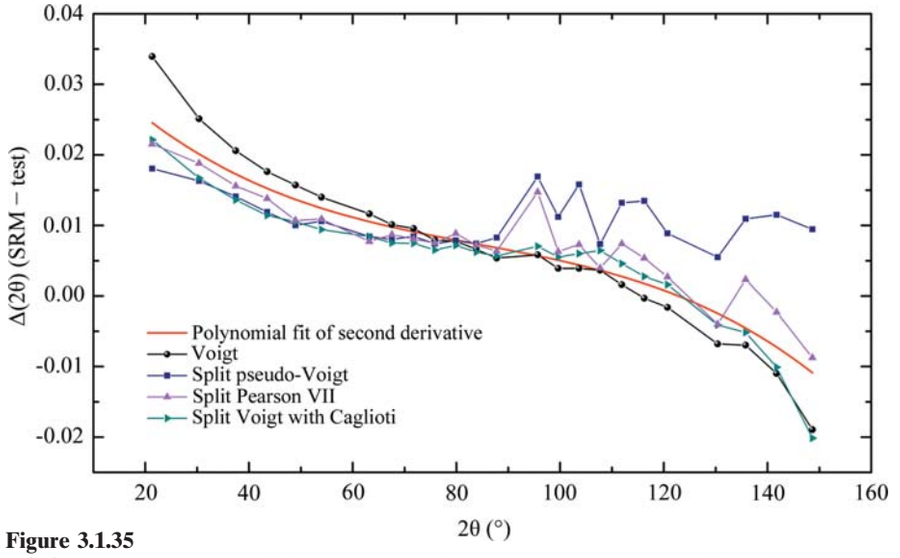

Figure 3.1.35
$\Delta(2\theta)$ curves from the NIST machine configured with a Johansson IBM, illustrating a comparison of results from second-derivative and various profile-fitting methods. Data are from SRM 660b.

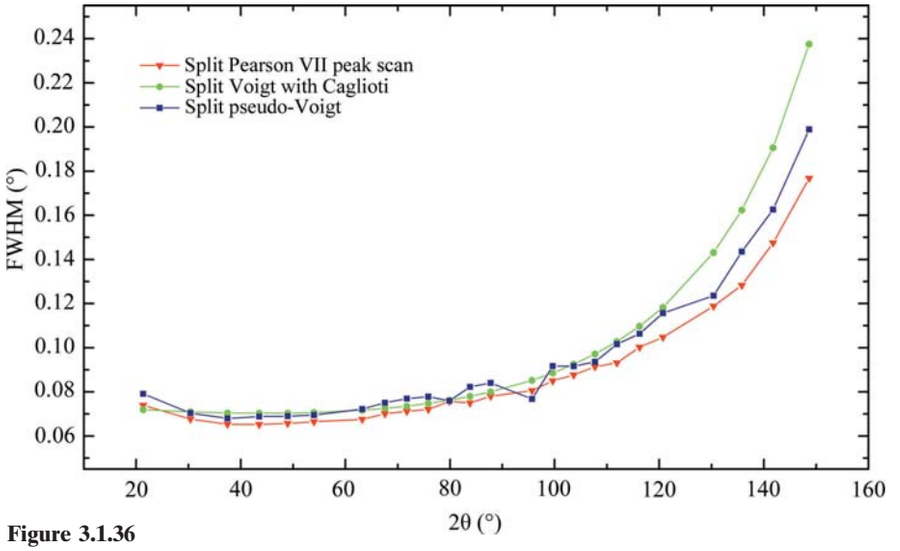

Figure 3.1.36
FWHM data from SRM 660b collected using the NIST machine configured with a Johansson IBM, illustrating a comparison of results from various profile-fitting and data-collection methods.

and, to a lesser extent, the split Pearson VII PSFs at high angle. However, the more accurate peak positions are obtained from the more intense reflections, indicating that higher-quality data may improve the results. Improvements in FWHM determination with the use of an IBM are illustrated in Fig. 3.1.36, where it can be seen that the pseudo-Voigt and Pearson VII yield values for the FWHM that differ in a systematic manner, but to a reduced extent than with the conventional data. The virtues of the peak-scan data are illustrated by the continuity of the FWHM values of Fig. 3.1.36 relative to the discontinuities observed in the corresponding data from the conventional scans that were fitted with the pseudo-Voigt PSF. The results from the use of the Caglioti function in Fig. 3.1.36 illustrate that otherwise noisy FWHM data are effectively smoothed out, but a significant bias at high angle is indicated.

FWHM values from the machine equipped with the IBM and PSD are shown Fig. 3.1.37, again with data from SRM 660b. These values were obtained from fits of the split Pearson VII PSF using uniform weighting. The resolution improvement from the use of the PSD is due to the 75 μm strip width, as opposed to the 200 μm receiving slit used with the scintillation detector. This is analogous to a reduction in the width of the top-hat function used to model the impact of the receiving slit or silicon strip width as discussed in Section 3.1.2. The impact is greatest at low 2θ angles where the other contributions to the overall breadth are small. With increasing 2θ angle, the contribution of a top-hat function to overall breadth is reduced because it is being convoluted with profiles influenced by ever-increasing spectral dispersion. The improve-

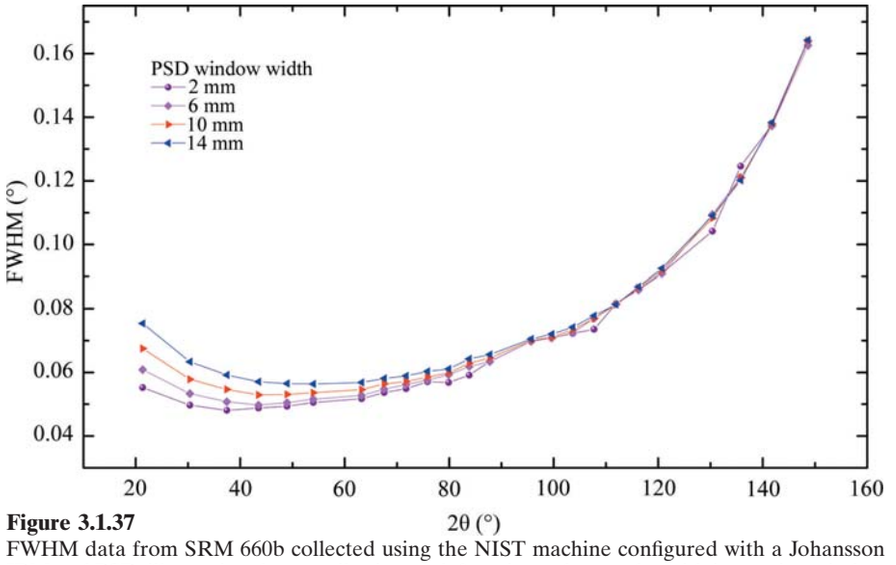

Figure 3.1.37
FWHM data from SRM 660b collected using the NIST machine configured with a Johansson IBM and PSD, illustrating the contribution to defocusing at low angles with increasing window width.

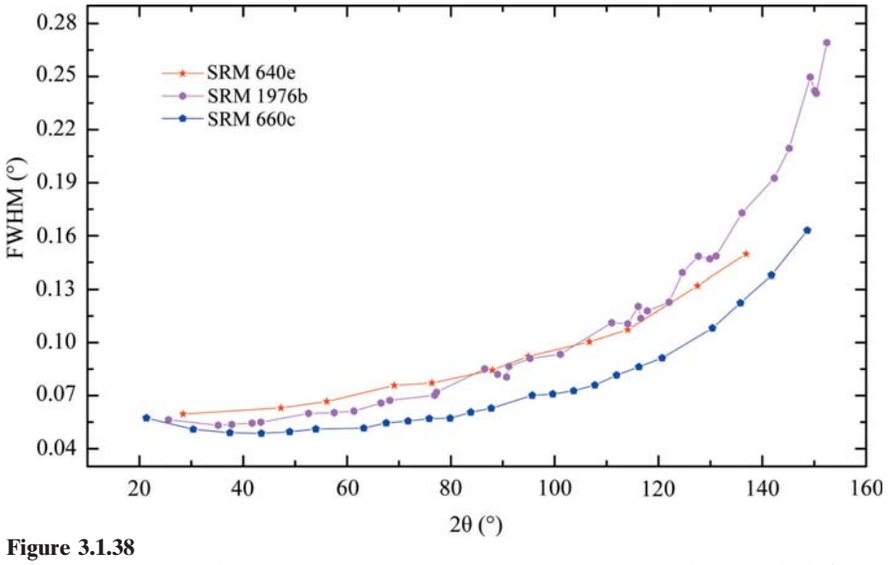

Figure 3.1.38
FWHM data from SRMs 640e, 1976b and 660c collected with the IBM and PSD (4 mm window) and fitted using the split Pearson VII PSF with uniform weighting.

ment in resolution with the reduction in the width of the PSD window is apparent, and is in accordance with expectations as per Fig. 3.1.7 of Section 3.1.2. Also, because of the $1/\tan\theta$ dependence of this broadening effect, the impact of the window size nearly vanishes above 100° 2θ.

Fig. 3.1.38 shows FWHM data obtained for SRMs 640e, 1976b and 660c using the split Pearson VII PSF, fitted using uniform weighting on data collected with the IBM and PSD with a 4 mm window. The 660c data set, which exhibits the lowest FWHM values, will be discussed first. The FPA analysis performed in the certifications of SRM 660b and 660c included a Lorentzian FWHM with a $1/\cos\theta$ dependence to account for size-induced broadening; a domain size of approximately 0.7 to 0.8 μm was indicated. There is a high level of uncertainty in these values, as they are reflective of an exceedingly small degree of broadening, the detection of which is near the resolution limit of the equipment. The term varying as $\tan\theta$, interpreted as microstrain, refined to zero. These values are found in the CoA for the SRMs. The linear attenuation coefficient for a compact of LaB_6, with an intrinsic linear attenuation of 1125 cm^{-1} and a particle-packing factor of 60 to 70%, would be approximately 800 cm^{-1}. Therefore, the contribution to the observed FWHM from specimen transparency with SRM 660c is negligible, as illustrated in Fig. 3.1.10. Likewise, the FPA analysis performed for the certification of SRM 640e included size and microstrain terms; a smaller crystallite size of 0.6 μm was obtained with a very slight amount of microstrain broadening. However, the linear attenuation coefficient for silicon is 148 cm^{-1}; for a powder compact it would be approximately 100 cm^{-1}. The transparency of this specimen would lead to significant broadening. (See Fig. 3.1.10 for the effect of an attenuation of 100 cm^{-1}.) Therefore, these three effects, in combination, would be expected to lead to a small degree of broadening throughout the 2θ range for SRM 640e, but with a substantial effect in the mid-angle region because of the $\sin 2\theta$ dependence of the transparency aberration. Lastly, SRM 1976b is a sintered compact of near theoretical density; therefore, considering the linear attenuation coefficient for alumina, 126 cm^{-1}, a value for the actual SRM 1976b specimen of somewhat less than this is expected. An FPA analysis of SRM 1976b indicates a domain size of 1 μm, but with a significant degree of Gaussian microstrain broadening; this is evident in the observed increase in FWHM with 2θ angle shown in Fig. 3.1.38. We conclude that the FWHM data from all three SRMs shown in Fig. 3.1.38 are in correspondence with expectations and can be used to select which SRM is best suited for a given application. We do not, however, recommend using an SRM other than SRM 660*x* for a microstructure analysis. It should be added that fitting the profiles of SRM 1976b is complicated by the fact that many of them overlap; this leads to the oscillations in the FWHM values shown in Fig. 3.1.38 for this SRM. The origins of this difficulty were discussed in Section 3.1.5 and can be addressed with the use of the Caglioti function.

With the use of model-based methods for calibration and subsequent data analysis, it is appropriate to consider a strategy for the refinement of the available parameters. The successful refinement will yield the right answer and, with the use of models that make sound physical sense with respect to the experimental design, a good fit to the observation. The refinement strategies for both FPA and Rietveld analyses can be based on a consideration of which terms are specific to the IPF and the manner in which they can be determined. Several parameters can be measured explicitly from experiments other than the diffraction experiment under examination. Examples of these 'well determined' parameters include the goniometer zero angles and the incident- and receiving-slit sizes. Conversely, indeterminate metrics that can only be determined through the diffraction experiment itself include the impact of the post-monochromator on the Cu $K\alpha_1/K\alpha_2$ ratio and the degree of axial divergence. Indeterminate parameters specific to the IPF are only refined using high-quality data from standards and are fixed for subse-

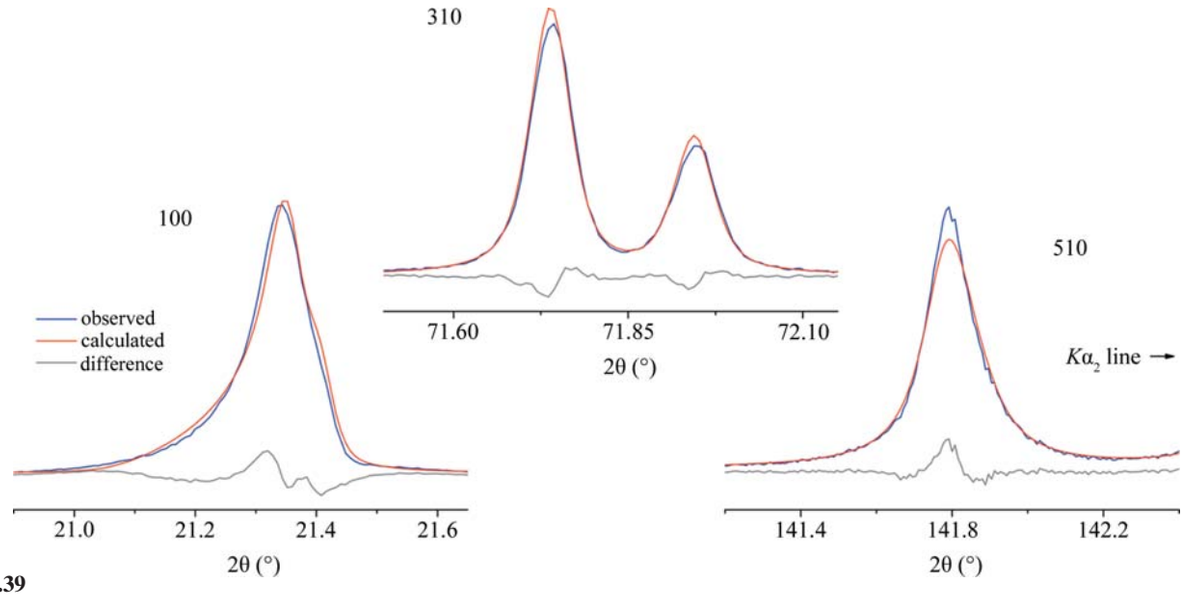

Figure 3.1.39
Fits of three SRM 660b lines obtained with a Rietveld analysis using the Thompson, Cox and Hastings formalism of the pseudo-Voigt PSF and the Finger model for asymmetry. *TOPAS* was used for the analysis.

quent analyses of unknowns. This approach tends to result in stable and robust refinements. Parameters can, therefore, be considered as falling into three groups: those that are specific to any given sample and are always refined, ones that are specific to the IPF and are refined using only high-quality data from standards, and lastly the highly determined parameters that are refined only as a basic test of the model.

To consider the Thompson, Cox & Hastings (1987) (TCH) formalism of the pseudo-Voigt PSF with the Finger model for asymmetry, which is common to many Rietveld codes, a Rietveld analysis of SRM 660b was performed using *GSAS* (using the type-3 PSF) and *TOPAS* (using the PV_TCHZ peak type). The TCH formalism allows for the direct refinement of the Gaussian and Lorentzian FWHM values. The Caglioti function was used; Lorentzian terms were constrained as per equation (3.1.2). The *S*/*L* and *H*/*L* terms are highly correlated; *S*/*L* was refined, while *H*/*L* was adjusted manually so that the two terms were nearly equal. Additional parameters that were refined included the lattice parameters, sample displacement and transparency terms, Chebyshev polynomial terms (typically 5 to 7) to represent the background, scale factors, the type-0 Lorentz–polarization term (*GSAS*), the Cu $K\alpha_1/K\alpha_2$ ratio, and structural parameters. With this strategy, the sample shift and transparency aberration functions, in conjunction with the Finger asymmetry model, were used to model the data of Fig. 3.1.26. Given that the Finger model is not entirely appropriate for divergent-beam laboratory data, the sample shift and transparency terms may refine to non-physical values. They will, however, correctly indicate relative values for sample *z* height and transparency. The model for specimen transparency in *TOPAS* is the asymmetric function illustrated in Fig. 3.1.10, while the model in *GSAS* consists of a profile displacement in $\sin 2\theta$. The TCH/Finger formalism of *TOPAS* reproduced the certified lattice parameter and resulted in a GoF of 1.5, whereas the GoF value realized with *GSAS* was 1.85. Fig. 3.1.39 displays the fit quality of the 100, 310 and 510 reflections obtained with *TOPAS*. The fit to the asymmetry of the 100 reflection is reasonable, with a 0.007° shift in position. The fit to the 510 reflection is not dissimilar to that shown in Fig. 3.1.32, indicating that the Caglioti function is working analogously to the manner previously discussed. The improvement in fit with the *TOPAS* implementation was most notable around the 70 to 90° 2θ region, where the transparency effects are at a maximum. These results validate the TCH/Finger formalism and constitute a valid calibration for this equipment and data-analysis method; the utility of the aberration function for specimen transparency as documented by Cheary & Coelho (1992) is demonstrated.

Differentiating between the profile-shape terms that are specific to the IPF and those refined to consider the microstructure of unknowns yields a stable refinement strategy when using the TCH/Finger formalism. The profile parameters *GU*, *GV*, *GW*, *LX*, *LY*, *S*/*L* and *H*/*L* as determined from SRM 660b constitute the IPF and are fixed, or used as floors, in subsequent refinements (Cline, 2000). The IPF for the NIST machine was described with only the *GW*, *LX* and *LY* parameters. In subsequent analyses only the *GP*, *GU*, *LX* and *LY* terms were refined to represent Gaussian size and microstrain and Lorentzian size and microstrain broadening, respectively, and thus yield microstructural information from the sample. Parameters that tend to values less than the IPF were fixed at IPF values. The Finger asymmetry parameters determined from the standard need not be refined with unknowns; it has, however, been observed that doing so will neither substantially improve the quality of the fit, nor will it result in instability. Additional parameters that are always refined with unknowns include: scale factors, lattice parameters, specimen displacement and transparency terms, background terms, and structural parameters.

While an analysis of SRM 660*x* permits the calibration of the instrument with respect to profile shape and position, it is also desirable to evaluate parameters related to the diffraction intensity. However, the analysis of data from high-symmetry materials such as silicon and lanthanum hexaboride may result in some degree of instability with the refinement of the intensity-specific parameters, perhaps because of the relatively small number of lines. Use of SRM 676a addresses this difficulty (Fig. 3.1.40). With this analysis, the Lorentz–polarization factor refined to a credible value and structure parameters were within the bounds of those obtained from the high-*q*-range experiments performed in the certification of SRM 676a (Cline *et al.*, 2011).

We start the discussion on the FPA method for instrument calibration by listing the parameters specific to the IPF that

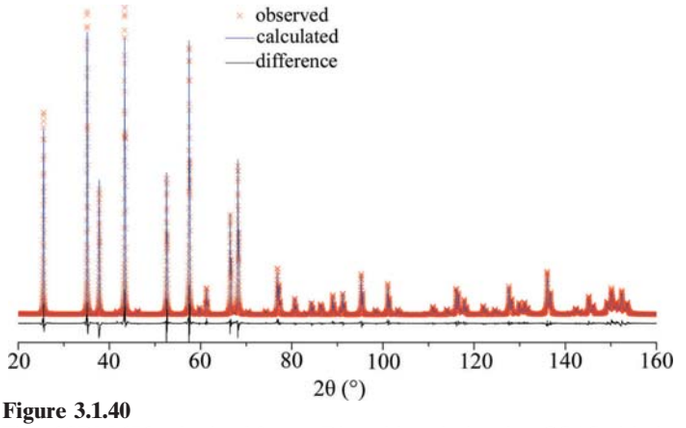

Figure 3.1.40
Fits of SRM 676a obtained from a Rietveld analysis using *GSAS* with the Thompson, Cox and Hastings formalism of the pseudo-Voigt PSF and the Finger model for asymmetry.

would have to be refined with a most basic calibration using an analysis of an SRM. The parameters to be refined for the emission spectrum include the positions and intensities of the $K\alpha_2$ profile, the satellite components and the tube tails. When addressing the $K\alpha_2$ profile, the relative positions and intensity ratios of the $K\alpha_{21}$ and $K\alpha_{22}$ Lorentzian profiles were constrained so as to preserve the overall shape as characterized by Hölzer *et al.* (1997). For the geometric profile, a single Soller-slit angle was refined, characterizing the degree of axial divergence and using the case-2 axial-divergence model applied to both the incident and diffracted beams. Other parameters of the geometric profile were fixed at known values. Additional parameters included a Lorentzian size-broadening term, background terms, and profile intensities and positions. A Gaussian microstrain term was included for analyses of SRM 1976b. Fig. 3.1.41 shows the quality of the fits obtained from an FPA analysis of SRM 660b. These fits present a substantial improvement over those using any of the analytical PSFs (Figs. 3.1.32 and 3.1.39). Furthermore, the GoF residual error term for an FPA profile analysis of a continuous scan of SRM 660b was 1.08, while the corresponding terms from analyses of the same data using the split pseudo-Voigt and split Pearson VII PSFs were 1.65 and 1.43, respectively (these three analyses were all from *TOPAS*). The FPA method can account for subtleties in the observed X-ray line profiles that analytical PSFs could never be expected to fit. In subsequent analyses of unknowns, it is not imprudent to fix parameters associated with the IPF; refining them, however, is typically not problematic with the FPA.

There were indications that the breadths of the profiles of the Cu $K\alpha$ emission spectrum as characterized by Hölzer *et al.* (1997) were in excess of those of our observations. This was investigated using the ultra-high-quality data. The FWHM ratios of the two pairs of Lorentzian profiles, the $K\alpha_{11}$ *versus* the $K\alpha_{12}$ and the $K\alpha_{21}$ *versus* the $K\alpha_{22}$, were constrained to those reported by Hölzer *et al.* (1997). The positions and intensities of the $K\alpha_2$ doublet were also refined, again with constraints applied to preserve the shape as per Hölzer *et al.* (1997). These refinements indicated that the breadths given by Hölzer *et al.* (1997) were significantly in excess of those that gave the best fit to the data. After an extensive investigation, this observation was confirmed to originate with the performance of the post-monochromator. Several graphite monochromator crystals were investigated using a beam diffracted from an Si single crystal (333 reflection) mounted in the specimen position. The graphite crystals that were manufactured within the last 15 years all gave identical results: after an alignment procedure to optimize the intensity of the $K\alpha_1$ line, they do clip the breadths of the profiles of the emission spectrum by approximately 20%. They also alter the position of diffraction lines by perhaps 0.01° in 2θ; therefore, the goniometer zero angles must be determined with the monochromator installed. We therefore used a reduced-breadth Hölzer emission spectrum in our FPA analysis. Note that these breadths vary with $\tan\theta$ because of angular dispersion, as does microstrain; therefore, only a microstrain-free specimen can be used for an analysis of the impact of a monochromator on the emission spectrum. We found that both SRMs 660c and 640e were suitable for this analysis.

The refinement strategy for the case-2 Soller-slit angle was also investigated with the ultra-high-quality data. Technically, the axial divergence of the incident beam, with the inclusion of the Soller slit, is less than that of the diffracted beam, which is limited by its extended beam-path length through the monochromator. Several strategies were investigated, some of which may have represented a more accurate physical model than that of a single divergence value applied to both beams, but none resulted in any improvement in the fit quality. Lastly, it was observed that the

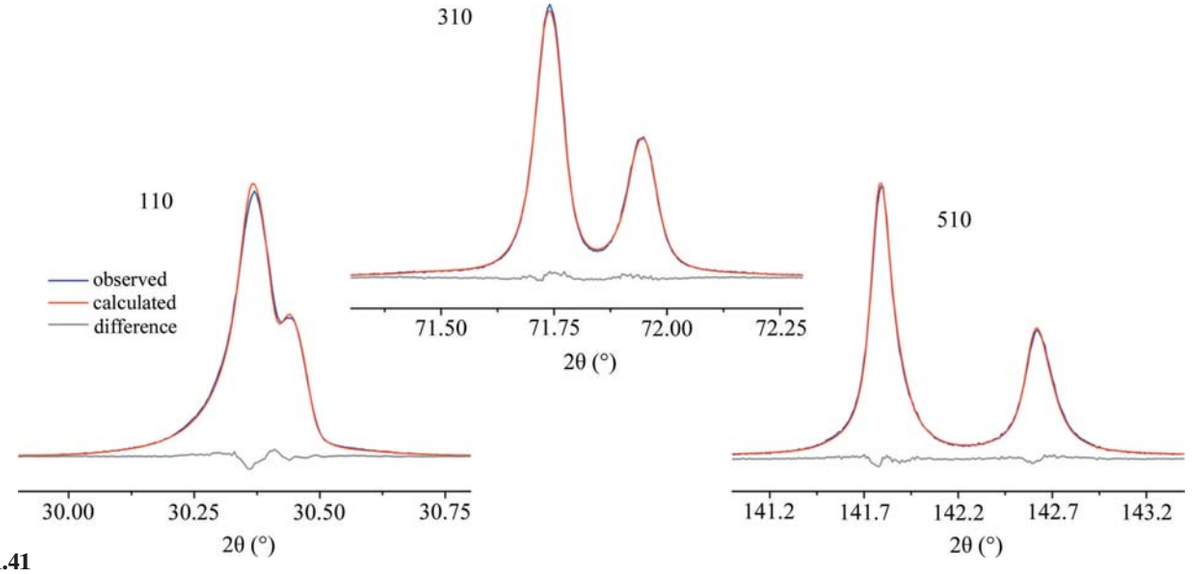

Figure 3.1.41
Fit quality realized with a fundamental-parameters-approach analysis of SRM 660b peak-scan data using *TOPAS*.

value for the width of the divergence slit, particularly with the use of the IBM, refined to values in excess of the known value. This observation will be discussed further.

With the certification of SRMs 640e, 660c and 1878b (respirable quartz, 2014), global refinements were set up allowing for the simultaneous analysis of the 20 high-quality data sets collected for the certification of each SRM. With this approach, the analyses could be carried out in the context of highly favourable Poisson counting statistics and permitted a robust analysis of FPA models that would otherwise be problematic because of parameter correlation. Data were collected from two samples from each bottle. With SRMs 640e and 660c, the machine was configured as per the work of this study with the post-monochromator; for 1878b, the machine was configured likewise with the IBM and scintillation detector. For SRM 660c the data were collected in accordance to the run-time parameters of Table 3.1.2, and in an analogous manner for SRM 640e. For SRM 1878b, the data were collected on mixtures of 50% SRM 1878b and 50% SRM 676a in continuous, 24 h scans. Concurrent with the effort to certify SRMs 640e and 660c, the agreement between the results from *FPAPC* and *TOPAS* was established, indicating that both codes operated in accordance with published FPA models (Mendenhall *et al.*, 2015). Initially with *FPAPC* and later with *TOPAS*, the data from these three SRMs were analysed using the global refinement strategy.

The global refinements were used to investigate possible difficulties with the FPA models. First, the global refinements were used to determine more robust values for the breadths of the emission spectrum as influenced by the post-monochromator. The issue concerning the refined value for the incident slit size was revisited with the global refinements. Values of 25% in excess of the known size were observed in refinements of IBM data from several materials using *TOPAS*. While these refinements were quite robust, corresponding analysis of ultra-high-quality post-monochromator data sets resulted in a slow increase in the slit value with little change in residual error terms, indicating a shallow χ^2 minimization surface. With the global analysis of the SRM 660c, 640e and 1878b data, however, the incident slit value refined to a value of 15 to 25% in excess of the known value in a robust manner. The reduced correlations between models with the global refinements led to this improved ability to reach the minimum in error space for both data types. An investigation into the sensitivity of the lattice-parameter value and GoF on the incident slit size was consistent with the shallow χ^2 minimization surface; changes in lattice parameters were less than 2 fm and only small changes in GoF were noted. The lowest-angle lines used in our analyses were at 18°; given the 1/tan θ dependence of the incident-slit correction, lower-angle lines are required for robust use of this model for refinement of incident-slit size. A second observation of concern was the low values for sample attenuation refined from data for SRM 660*x*. As previously stated, a reasonable value for a compact of LaB_6 would be 800 cm^{-1}, yet the fits were giving values in the 400 cm^{-1} range. Again, a sensitivity study indicated little dependence of either the lattice parameter or the GoF on the attenuation values when they are this large. In contrast, sensitivity studies on SRM 640*x* (silicon in the 80 to 100 cm^{-1} range) indicated a high level of response to changes in attenuation values. Again, in the range where the model is active, results are in correspondence with expectations; where there is little impact on the refinement, parameter values may differ from true values with little impact on the refinement as a whole. We are continuing to investigate the issue of the non-physical values obtained for the refined divergence-slit width.

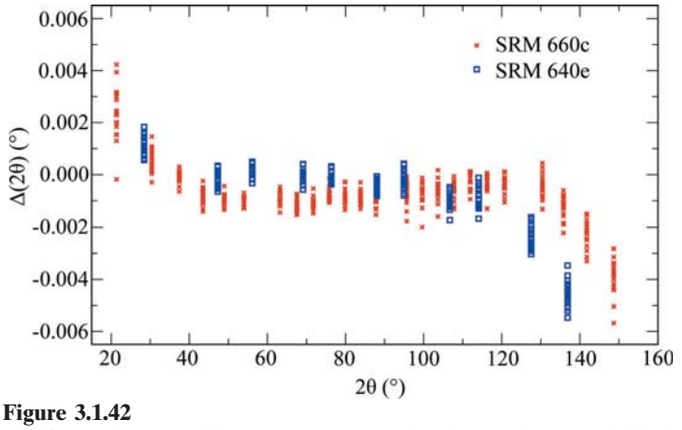

Figure 3.1.42
$\Delta(2\theta)$ data from the 20 data sets collected for the certification of SRMs 660c and 640e, determined *via* FPA analyses using *TOPAS*.

The $\Delta(2\theta)$ data shown in Fig. 3.1.42 illustrate results from an FPA analysis of the 20 data sets collected for the certification of SRMs 660c and 640e. The $\Delta(2\theta)$ values were generated using the certified lattice parameters of SRMs 660c and 640e to compute 'SRM' or reference peak positions, and the unconstrained profile positions from the FPA analysis were used as the 'test' data. The analyses were performed using *TOPAS* with the divergence-slit width fixed at the known value. The data in Fig. 3.1.42 clearly reflect the efficacy of the FPA method. The certification data for these SRMs were collected on the machine set up as for Fig. 3.1.26; the trends of the peak position for these data are identical to those of Fig. 3.1.26. Yet the FPA has corrected the profile positions to a degree indiscernible from the 'true' positions in the 40 to 120° 2θ region. The trends observed otherwise in these data are consistent with prior observations discussed at length above, albeit in 2θ regions limited to below 40° and above 120° and to a vastly reduced level. These deviations are consistent with shortcomings in the model, although the deviations are so small that it may be difficult to work out their origin. The unequivocal technical justification for use of the FPA in SRM certification is also apparent in Fig. 3.1.42; when properly used, the method is capable of reporting the 'true' *d*-spacing for profiles located in the 40 to 120° 2θ region.

Using SRM 1976b for calibration of the instrument response entails determining the integrated intensity of 14 profiles from the test instrument and comparing them with certified values. However, the test instrument in this case was the NIST instrument equipped with the graphite post-monochromator. Therefore, the relative intensity values used for comparison were the ones biased to account for the effects of polarization. They were obtained from Table 4 of the SRM 1976b CoA. Fig. 3.1.43 shows the results from various data-analysis techniques performed on a common raw data set from the test instrument. With the noteworthy exception of the split Pearson VII PSF, all methods gave an acceptable result. It can be seen that when intensity measurement is the issue, the use of unconstrained PSFs is more effective than the analyses described earlier, which were intended to determine the profile position or FWHM. With the use of *GSAS*, the pattern was fitted with a Rietveld analysis using a sixth-order spherical harmonic to model the texture. The reported relative intensity data are computed from the observed structure factors using the *GSAS* utility *REFLIST*. This approach is identical to that used for the certification of SRM 1976b, except the certification data were collected on the NIST instrument setup with the IBM.

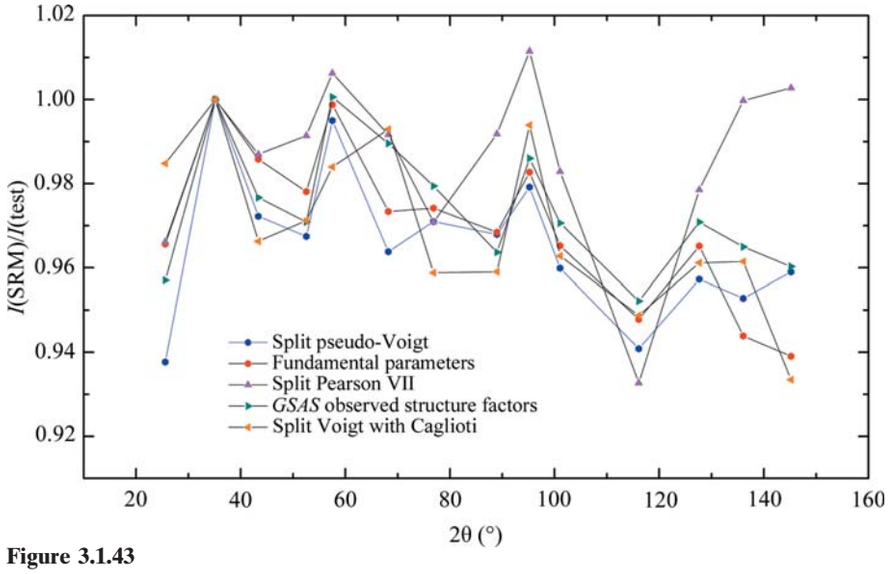

Figure 3.1.43
Qualification of a machine using SRM 1976b. The data were analysed using several PSFs.

The structure common to all the data sets of Fig. 3.1.43 is as yet unexplained. With any of these methods, modelling the background is of critical concern. The intensity scale of the fitted pattern must be expanded to allow for inspection of the background fit alone. The weak amorphous peak at approximately 25° 2θ, which is associated with the anorthite glass matrix phase, complicates the matter. Certain refinement programs allow for the insertion of a broad peak to account for this. Alternatively an 11- to 13-term Chebyshev polynomial could be used. Keeping the number of these terms to a minimum is consistent with preventing the background function from interfering with the modelling of the profiles. Lastly, the use of $K\beta$ filters in conjunction with a PSD can be problematic for the calibration of instrument response using SRM 1976b. Such filters typically impart an absorption edge in the background on the low-energy side of the profiles. With the use of a high-count-rate PSD, this effect can be quite pronounced and can cause difficulties in fitting the background and, therefore, erroneous determination of the profile intensity.

3.1.7. Conclusions

In this chapter, we reviewed the theoretical background behind the well known complexity of X-ray powder diffraction line profiles. A divergent-beam laboratory X-ray diffractometer with a conventional layout was used to rigorously examine the full range of procedures that have been developed for the analysis of the instrument profile function. The machine featured superlative accuracy in angle measurement, and attention was paid to the precision and stability of the optical components and sample positioning. The instrument was aligned in accordance with first-principles methods and was shown to exhibit an optical performance that conformed with the expectations of established theories for powder-diffraction optics.

Data-analysis methods can be divided into two categories that require fundamentally different approaches to instrument calibration. Empirical profile-analysis methods, either based on second-derivative algorithms or profile fitting using analytical profile-shape functions, seek to characterize the instrument performance in terms of shape and position parameters that are used in subsequent analysis for determining the character of the specimen. These methods, however, provide no information about the origins of the peak shift or profile shape that they describe. Model-based methods seek to link the observation directly to the character of the entire experiment. The calibration procedure for the first category can be regarded as a 'classical' calibration where a correction curve is developed through the use of an SRM and applied to subsequent unknowns. With model-based methods, it is the user's responsibility to calibrate the instrument in a manner that ensures that the models that are being used correctly correspond to the experiment. This is best accomplished through the analysis of results from empirical methods, particularly $\Delta(2\theta)$ curves, as well as the analysis of data from an SRM followed by a critical examination of the refined parameters.

Second-derivative-based algorithms for determining peak locations are able to provide the 2θ positions (the positions of the maxima in the observed profile intensity) to within $\pm 0.0025°$ 2θ. Profile fitting using analytical profile-shape functions to determine the peak position was shown to be problematic; errors of up to 0.015° 2θ were noted. The use of uniform weighting in the refinements resulted in improved accuracy in the reported peak positions and FWHM values. Using a Johansson incident-beam monochromator led to high-quality fits of diffraction data using analytical profile shape functions. The Caglioti function can be used to improve the reliability of FWHM values.

The fundamental-parameters approach was found to be effective in modelling the performance of the Bragg–Brentano divergent-beam X-ray diffractometer. The form of the $\Delta(2\theta)$ curve, determined *via* a second-derivative algorithm, can be explained quantitatively through an examination of FPA models. Furthermore, FPA simulations of diffraction data, computed from the instrument configuration using both commercial and NIST FPA codes, and analysed using the same second-derivative algorithm, reproduced the $\Delta(2\theta)$ results from the experimental data. This self-consistency verified the correct operation of both the instrument and the FPA models. Using the FPA for modelling the diffraction profiles provided the best fits to the observations and the most accurate results for the 'true' reported peak positions. The TCH/Finger models for profile shape yielded credible results for refinement of lattice parameters *via* the Rietveld method.

This chapter is based on an article published in the *Journal of Research of the National Institute of Standards and Technology* (Cline *et al.*, 2015).

References

Azároff, L. V. (1955). *Polarization correction for crystal-monochromatized X-radiation*. *Acta Cryst.* **8**, 701–704.
Bergmann, J., Friedel, P. & Kleeberg, R. (1998). *BGMN – a new fundamental parameters based Rietveld program for laboratory X-ray sources, it's use in quantitative analysis and structure investigations*. *IUCr Commission on Powder Diffraction Newsletter*, **20**, 5–8. http://www.iucr.org/resources/commissions/powder-diffraction/newsletter/.
Bergmann, J., Kleeberg, R., Haase, A. & Breidenstein, B. (2000). *Advanced fundamental parameters model for improved profile analysis*. In *Proceedings of the Fifth European Conference on Residual Stresses*, edited by A. J. Böttger, R. Delhez & E. J. Mittemeijer, *Mater.*